

# UC Santa Barbara

## UC Santa Barbara Previously Published Works

### Title

Nucleation of the destruction complex on the centrosome accelerates degradation of  $\beta$ -catenin and regulates Wnt signal transmission

### Permalink

<https://escholarship.org/uc/item/08w8q3gv>

### Journal

Proceedings of the National Academy of Sciences of the United States of America, 119(36)

### ISSN

0027-8424

### Authors

Lach, Ryan S  
Qiu, Chongxu  
Kajbaf, Erfan Zeyaei  
et al.

### Publication Date

2022-09-06

### DOI

10.1073/pnas.2204688119

Peer reviewed



# Nucleation of the destruction complex on the centrosome accelerates degradation of $\beta$ -catenin and regulates Wnt signal transmission

Ryan S. Lach<sup>a</sup>, Chongxu Qiu<sup>a</sup>, Erfan Zeyaei Kajbaf<sup>a</sup>, Naomi Baxter<sup>a</sup>, Dasol Han<sup>b</sup>, Alex Wang<sup>a</sup>, Hannah Lock<sup>a</sup>, Orlando Chirikian<sup>c</sup>, Beth Pruitt<sup>a,d,e</sup>, and Maxwell Z. Wilson<sup>a,b,c,e,1</sup>

Edited by Mariann Bienz, MRC Laboratory of Molecular Biology, Cambridge, United Kingdom; received March 17, 2022; accepted July 27, 2022 by Editorial Board Member Janet Rossant

Wnt signal transduction is controlled by the destruction complex (DC), a condensate comprising scaffold proteins and kinases that regulate  $\beta$ -catenin stability. Overexpressed DC scaffolds undergo liquid–liquid phase separation (LLPS), but DC mesoscale organization at endogenous expression levels and its role in  $\beta$ -catenin processing were previously unknown. Here, we find that DC LLPS is nucleated by the centrosome. Through a combination of CRISPR-engineered custom fluorescent tags, finite element simulations, and optogenetic tools that allow for manipulation of DC concentration and multivalency, we find that centrosomal nucleation drives processing of  $\beta$ -catenin by colocalizing DC components to a single reaction crucible. Enriching GSK3 $\beta$  partitioning on the centrosome controls  $\beta$ -catenin processing and prevents Wnt-driven embryonic stem cell differentiation to mesoderm. Our findings demonstrate the role of nucleators in controlling biomolecular condensates and suggest tight integration between Wnt signal transduction and the cell cycle.

Wnt | destruction complex | optogenetics | LLPS | stem cells

The canonical Wnt signaling pathway is a conserved (1), morphogenic pathway that is essential for embryonic development, maintains adult tissue homeostasis, and, when dysregulated, induces malignancies (2–4). Wnt signals converge onto a protein assembly called the destruction complex (DC), which tunes the stability of  $\beta$ -catenin ( $\beta$ -cat), the pathway's central transcriptional effector, by regulating its interactions with the kinases, CK1 $\alpha$  and GSK3 $\beta$ , and the ubiquitinase,  $\beta$ -TRCP, which directs  $\beta$ -cat to the ubiquitin-mediated proteolysis machinery. Despite the DC's role in regulating  $\beta$ -cat stability, the structural principles that underlie its functioning in development and disease are still poorly understood.

Extracellular Wnt ligands inhibit DC function through a mechanism that is still unclear, but likely involves selective recruitment of DC components to the signalosome, a biomolecular condensate on the plasma membrane that includes Wnt/Frizzled/LRP5/6 clusters (5). Optogenetic clustering of LRP5/6 is sufficient to stabilize  $\beta$ -cat (6), suggesting the formation of mesoscale protein clusters at the Wnt receptor level is necessary and sufficient for activating the pathway. Less is known about the DC's native structure and how it maintains low  $\beta$ -cat levels in the Wnt OFF state. Recently, the DC scaffolds Axin and Adenomatous Polyposis Coli (APC), and the signalosome “adapter” protein Disheveled have been shown to undergo liquid–liquid phase separation (LLPS) in vitro (7) and, when exogenously overexpressed, in vivo (8–10). Cancer-causing mutations that eliminate Axin or APC LLPS are correlated with aberrant accumulation of  $\beta$ -cat (11, 12) and can be rescued by orthogonal protein-multimerizing domains (13). These studies raise the question, What is the role of mesoscale assembly of the cytoplasmic DC components in regulating  $\beta$ -cat stability?

The “molecular crucible” model posits that DC LLPS promotes  $\beta$ -cat degradation in Wnt OFF conditions (7) via concentration of DC clients (CK1 $\alpha$ , GSK3 $\beta$ , and  $\beta$ -cat) in DC scaffold (Axin and APC) condensates to increase the rate of  $\beta$ -cat processing. LLPS-mediated DC concentration is distinct from theories suggesting that the DC acts as an ordered, assembly line–like scaffold akin to Ste5 in the yeast MAPK pathway (14). Indeed, deletions in Axin regions that promote LLPS (15) increase  $\beta$ -cat stability (7). In this paradigm, conditions that alter the phase behavior of scaffolds and partitioning of clients are predicted to regulate the stability of  $\beta$ -cat and Wnt signal transmission.

A biophysical mechanism for regulating condensates is control over their nucleation. This principle was recently explored with a synthetic optogenetic system (16), but the role of nucleation in natural biological processes remains unknown. Phase-separating systems exhibit switch-like responses to changes in concentration (17, 18) and often

## Significance

Liquid–liquid phase separation (LLPS) governs a variety of mesoscale cellular processes. However, less is known about how cells utilize LLPS to drive cellular function. Here, we examined the destruction complex (DC), an organelle which controls Wnt signaling and whose components phase separate. Through a combination of advanced microscopy, CRISPR, computational modeling, and optogenetics, we find that the DC is nucleated by the centrosome and that this nucleation drives efficient signal transduction. Our work not only uncovers a biological function for LLPS but also highlights nucleation as a general method for controlling the function of intracellular condensates. Finally, our findings suggest a thermodynamic coupling between Wnt signal transduction and the cell cycle which could lead to insights into Wnt-driven cancers.

Author contributions: B.P. and M.Z.W. designed research; R.S.L., C.Q., E.Z.K., N.B., D.H., A.W., H.L., and O.C. performed research; R.S.L., C.Q., E.Z.K., D.H., A.W., and H.L. analyzed data; and R.S.L. and M.Z.W. wrote the paper.

The authors declare no competing interest.

This article is a PNAS Direct Submission. M.B. is a guest editor invited by the Editorial Board.

Copyright © 2022 the Author(s). Published by PNAS. This open access article is distributed under Creative Commons Attribution License 4.0 (CC BY).

See online for related content such as Commentaries.

<sup>1</sup>To whom correspondence may be addressed. Email: mzw@ucsb.edu.

This article contains supporting information online at <http://www.pnas.org/lookup/suppl/doi:10.1073/pnas.2204688119/-DCSupplemental>.

Published August 29, 2022.

exist near these transitions in vivo (19, 20). Dissecting the mechanisms controlling LLPS requires control over protein concentration and affinity, and overexpression of DC components may not recapitulate endogenous mesoscale structure. Here, we utilize CRISPR gene editing, custom inducible expression vectors, and optogenetic tools to observe and probe the native, mesoscale organization of the DC in the Wnt OFF and Wnt ON states.

Building on results demonstrating that  $\beta$ -cat (21, 22), Axin1 (23), APC (24), and  $\beta$ TrCP/*Slimb* (25) localize to the centrosome, we show that all DC components are nucleated by the centrosome into liquid-like biomolecular condensates. In support of the molecular crucible theory, we find that nucleation drives efficient degradation of  $\beta$ -cat. We utilize a Cahn–Hilliard-based simulation of DC droplet formation and enzyme kinetics to predict how nucleation and affinity of DC components promotes efficient  $\beta$ -cat processing. Finally, using our model as a guide, we engineered a light-inducible GSK3 $\beta$  (Opto-GSK3) to control partitioning at the centrosome,  $\beta$ -cat degradation, and stem cell differentiation into mesoderm. These findings show that DC droplet formation is nucleated by the centrosome and suggest that DC scaffolds function to concentrate clients in liquid droplets in vivo to accelerate the degradation of  $\beta$ -cat.

## Results

### $\beta$ -Cat Condensation Is Predictive of Wnt Pathway Activity

**State.** To understand the role of mesoscale organization in DC function, we first sought to characterize the DC's main substrate,  $\beta$ -cat in live cells. We used CRISPR to knock in a custom fluorescent tag, tdmRuby3, to the *CTNNB1* gene of 293T cells (Fig. 1A). Live-cell confocal imaging revealed expected cytoplasmic accumulation in response to Wnt-3a ligand and the GSK3 $\beta$  inhibitor CHIR (*SI Appendix, Fig. S1 A and B and Movie S1*) and localization of  $\beta$ -cat at the cell membrane, consistent with previous work in fixed specimens (26). In addition, we observed that most cells contained one or two bright, spherical, perinuclear  $\beta$ -cat puncta (Fig. 1B). Timelapses showed fission and fusion of puncta on the timescale of minutes (Fig. 1M), suggesting that these structures are liquid-like biomolecular condensates. Given the prevalence of biomolecular condensates in organizing important biological processes, we hypothesized that these perinuclear puncta might organize  $\beta$ -cat destruction.

To determine whether Wnt pathway activation altered the perinuclear puncta, we performed volumetric confocal timelapse microscopy on our *tdmRuby3- $\beta$ -cat* cells and quantified the fraction of cells with puncta as a function of Wnt-3a ligand treatment and time. At the population level, the fraction of cells with puncta significantly decreased in response to Wnt-3a (Fig. 1C). We found this same relationship existed between single cells in an isogenic population: nonresponding cells maintaining their puncta and responding cells dissolving them (Fig. 1D and E). Thus, the disappearance of perinuclear  $\beta$ -cat puncta is correlated with  $\beta$ -cat accumulation, and the existence of these puncta is correlated to the resistance of ligand-induced accumulation.

To establish whether directly activating the Wnt receptor controls the existence of the puncta, we transduced *tdmRuby3- $\beta$ -cat* cells with an optogenetic version of the Wnt coreceptor, LRP6c (Opto-LRP6) (6). Opto-LRP6 induced greater accumulation of  $\beta$ -cat than either Wnt or CHIR (Fig. 1K and L). We thus reasoned that this all-optical Wnt input control and output visualization cell line would maximize our ability to observe rearrangements in pathway components due to a higher dynamic range of activation (Fig. 1F). We found that activating Opto-LRP6

resulted in a greater reduction in the fraction of cells containing  $\beta$ -cat puncta than treating cells with ligand (Fig. 1G and H and *Movies S2 and S3*).  $\beta$ -cat puncta became more difficult to distinguish at higher cytoplasmic concentrations produced by activated Opto-LRP6, but dissolution nearly always preceded appreciable dilute-phase  $\beta$ -cat accumulation, indicating that they were not simply obscured by higher background levels. Further, of light-stimulated cells, those that were resistant to optogenetic activation maintained their  $\beta$ -cat puncta (Fig. 1I and J). We also observed this same resistance to  $\beta$ -cat accumulation in response to CHIR (*SI Appendix, Fig. S1B*). Together, these results indicate that activation of the Wnt pathway causes perinuclear puncta to dissolve, and the presence of these puncta is inversely related to Wnt pathway activation at the population and single-cell levels.

### The DC Forms a Biomolecular Condensate Colocalized to the Centrosome.

We next sought to determine 1) what, if any, cellular structure was organizing these puncta, 2) whether all DC components were colocalized with puncta, and 3) whether these were solid or liquid-like condensates. Because of the sensitivity of LLPS systems to protein concentration (27), we decided on a strategy that allowed for visualization of DC components at low or endogenous concentrations, while retaining the ability to assess protein dynamics through live-cell microscopy and fluorescence recovery after photobleaching (FRAP). Indeed, DC scaffolds APC and Axin1 form multiple liquid droplets when overexpressed (12, 28). Thus, we used CRISPR to knock in *tdmRuby3* into the loci of *CSNK1A1*, *GSK3B*, and *AXIN1*, genes encoding the kinases CK1 $\alpha$  and GSK3 $\beta$  that sequentially phosphorylate  $\beta$ -cat in the DC, and the primary DC scaffold.

We found that all tagged proteins were localized into one or two perinuclear puncta (Fig. 2A). Timelapses revealed that the number and position of the puncta were determined by cell cycle stage (*SI Appendix, Fig. S2A*): We observed single condensates in G1, two condensates in G2/S, and a “finger-like” pattern—suggesting association with the mitotic spindle—during late mitosis. These observations, combined with previous reports of perinuclear enrichment of CK1 $\alpha$ , GSK3 $\beta$ , and Axin1 in fixed cells (29–31), led us to hypothesize that these DC components and  $\beta$ -cat were associated with the centrosome. Immunofluorescence staining for  $\gamma$ -tubulin (Fig. 2B) and GM130 (*SI Appendix, Fig. S2B*) confirmed that *tdmRuby3-CK1 $\alpha$* , *tdmRuby3-GSK3 $\beta$* , and *tdmRuby3- $\beta$ -cat* puncta were indeed colocalized to the centrosome.

When overexpressed, Axin and APC cross the phase boundary and form liquid condensates in the cytoplasm that are hypothesized to concentrate DC kinases and  $\beta$ -cat (32). The fact that no extracentrosomal DC puncta were observed in cells at endogenous concentrations led us to hypothesize that the DC is a liquid organelle that is nucleated at the centrosome at endogenous protein concentrations, but forms extracentrosomal condensates at higher concentrations. To test whether Axin1 and APC are localized to the centrosome at low cellular concentrations, but not when overexpressed, we generated clonal 293Ts bearing doxycycline (Dox)-inducible human Axin1-*tdmRuby3* and cumate-inducible human APC-*tdmRFP670*. At low levels of induction, both Axin1 and APC localization mirrored CRISPR CK1 $\alpha$ , GSK3 $\beta$ , Axin1, and  $\beta$ -cat, forming bright perinuclear puncta (Fig. 2C, *Left*) that colocalized with centrosomal markers (Fig. 2D and *SI Appendix, Fig. S2B*) and replicated following cell cycle progression (*SI Appendix, Fig. S2A*). As protein concentration increased, Axin1, but not APC, caused formation of extracentrosomal puncta throughout the cytoplasm (Fig. 2C–E). To determine whether extracentrosomal condensates observed at high Axin1 concentrations were capable

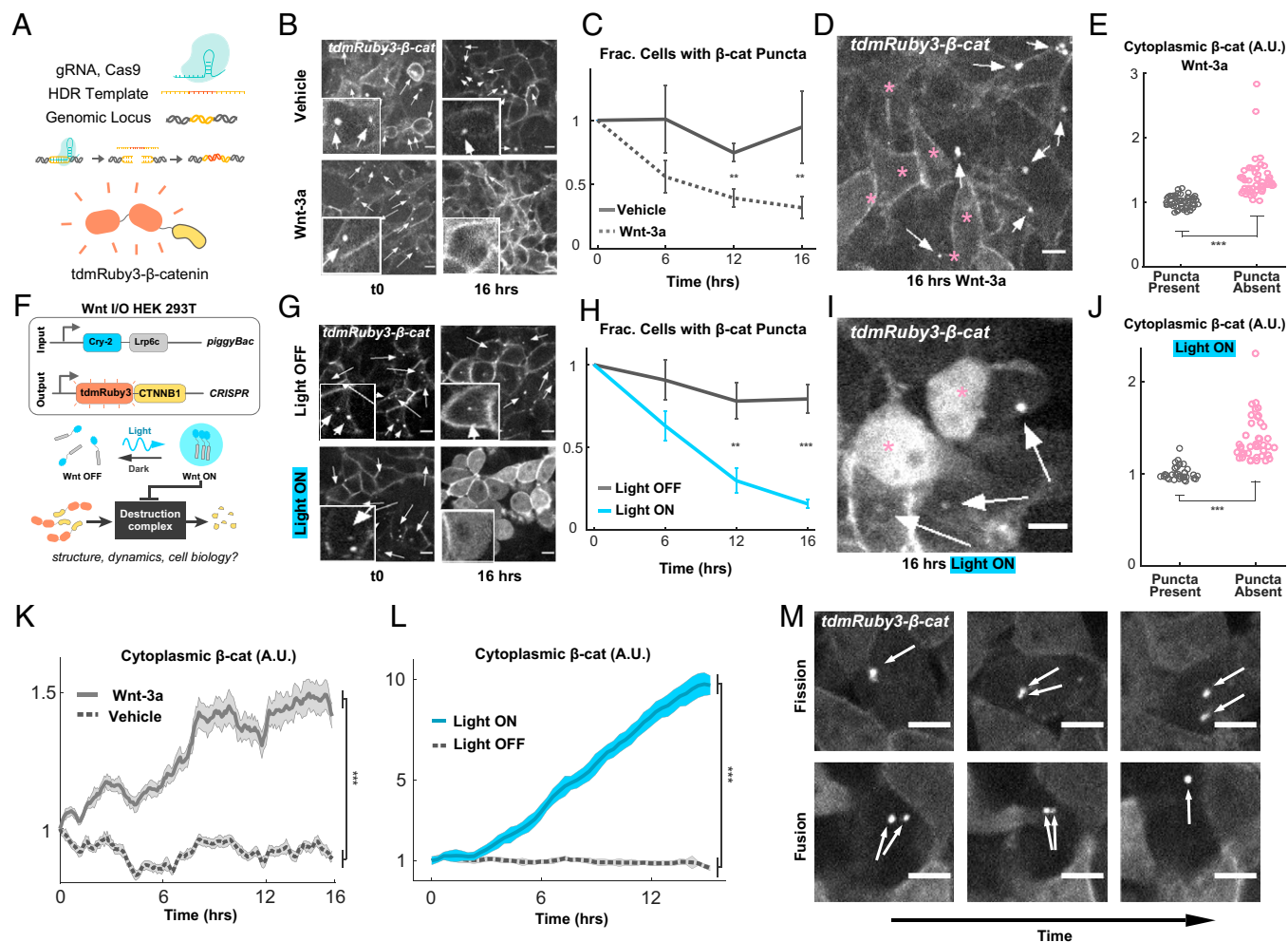


**Fig. 1.** Endogenously expressed  $\beta$ -cat puncta are inversely correlated with Lrp6-mediated Wnt pathway activation and  $\beta$ -cat accumulation. (A) Schematic of tdmRuby3 CRISPR tag strategy. (B) Representative tdmRuby3- $\beta$ -cat images of cells treated with Wnt-3a or media vehicle. Arrows indicate  $\beta$ -cat puncta. (Scale bars, 10  $\mu$ m.). Insets show closeup examples of presence (arrows) or lack of puncta. (C) Fraction of t0 population with visible  $\beta$ -cat puncta, presented as mean  $\pm$  SEM ( $n = 12$  imaging fields per condition). (D) Representative cells from Wnt-3a condition. Arrows indicate puncta, and asterisks indicate cells lacking puncta. (Scale bars, 10  $\mu$ m.). (E) Comparison of mean cytoplasmic  $\beta$ -cat fluorescence between Wnt-3a cells with and without visible  $\beta$ -cat puncta. (F) Schematic of Wnt I/O cells containing lentivirally expressed Cry2-LRP6c and CRISPR-tagged tdmRuby3- $\beta$ -cat. Stimulation of Cry2-Lrp6c with blue light results in reversible clustering of Lrp6c and downstream pathway activation. (G) Representative tdmRuby3- $\beta$ -cat images of cells stimulated with blue light or left in the dark throughout imaging time course. Insets show closeup examples of presence (arrows) or lack of puncta. (Scale bars, 10  $\mu$ m.). (H) Fraction of t0 population with visible  $\beta$ -cat puncta, presented as mean  $\pm$  SEM ( $n = 12$  imaging fields per condition). (I) Representative cells from Wnt-3a condition. Arrows indicate puncta, and asterisks indicate cells lacking puncta. (Scale bars, 10  $\mu$ m.). (J) Comparison of mean cytoplasmic  $\beta$ -cat fluorescence between Light ON cells with and without visible  $\beta$ -cat puncta. (K and L) Measurements of CRISPR cytoplasmic tdmRuby3- $\beta$ -cat in live 293Ts; data presented as mean fluorescent intensity fraction of t0  $\pm$  SEM ( $n = 30$  cells per condition). (M) Time course montage of single CHIR+ cells containing  $\beta$ -cat puncta undergoing dynamic fission and fusion. Arrows indicate puncta. Images are from consecutive frames of time course, separated by 5-min intervals. (Scale bars, 10  $\mu$ m.)

of concentrating canonical DC components similar to centrosomal DCs, we next expressed Dox-Axin1-GFP in CRISPR tdmRuby3-CK1 $\alpha$  and GSK3 $\beta$  backgrounds. Cells with high Axin1 levels formed extracentrosomal condensates colocalized with APC, CK1 $\alpha$ , and  $\beta$ -cat (*SI Appendix, Fig. S2E*). Interestingly, extracentrosomal Axin1 condensates did not reliably induce formation of extracentrosomal GSK3 $\beta$  condensates in these experiments, but often resulted in deenrichment of centrosomal puncta (*SI Appendix, Fig. S2E*). We reason that this was due to extracentrosomal Axin1 condensates competing for relatively scarce GSK3 $\beta$ , thereby diluting across all condensates in the cytoplasm.

The 293Ts are commonly used in experiments probing DC mesoscale structure in vivo (7, 10), but expression of Wnt pathway components may vary significantly between stem cells and differentiated cells. We observed the same preferential localization of Axin1 at low concentration in human induced pluripotent stem cells (hiPSCs) (*SI Appendix, Fig. S2F*). These findings establish that all DC components necessary for phosphorylating

$\beta$ -cat, prior to its ubiquitination, are localized at the centrosome throughout the cell cycle and suggest that DC centrosomal nucleation is generalizable to multiple cell types.

Next, we sought to determine the material state of the centrosomal DC using FRAP on CRISPR-tagged CK1 $\alpha$ , GSK3 $\beta$ , and  $\beta$ -cat, as well as of Axin1 and APC at low levels of induction. All centrosomal DC components exhibited mean half-maximal recovery times ( $\tau/2$ ) between 10 s and 60 s (Fig. 2E)—like in over-expressed systems (15) and in line with mesoscale cellular structures considered liquid-like (33). Interestingly, relatively wide variation in both stable fraction and  $\tau/2$  was observed between centrosomal DC components, indicating differential turnover of monomers between condensates and the bulk cytoplasm. This suggests that multiple biophysically distinct pools of each component, with different condensation dynamics, coexist at the centrosome together. Despite this, these results support the idea that the DC is a liquid nucleated by the centrosome and suggest that nucleation has a role in maintenance of cellular  $\beta$ -cat levels.

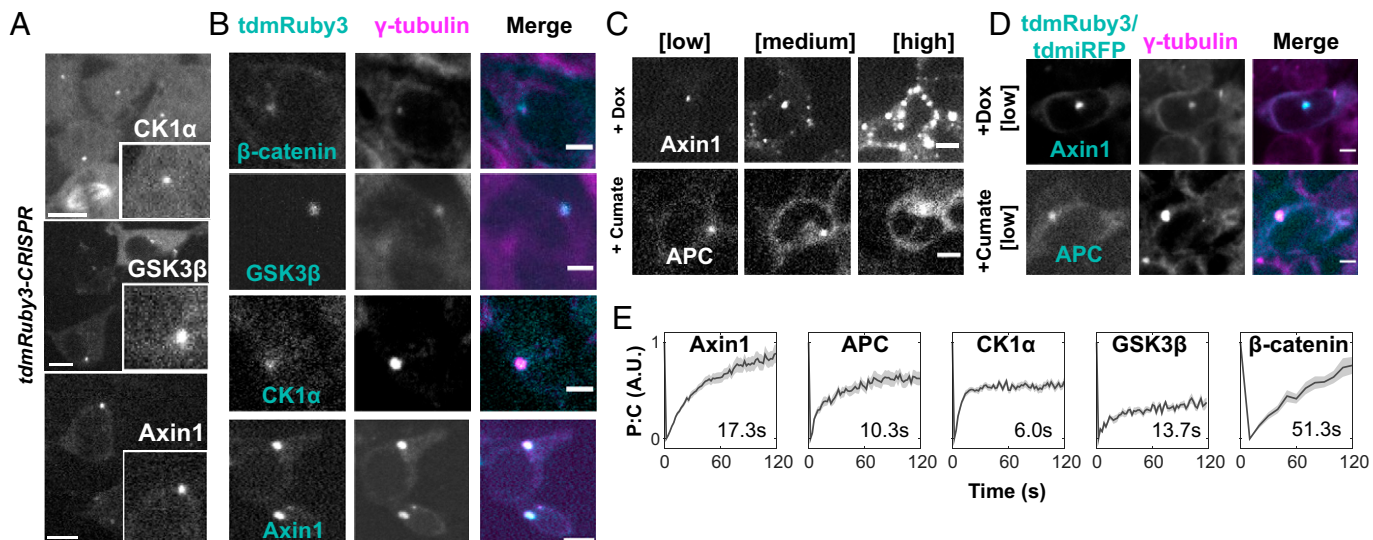


**Fig. 2.** Canonical DC components reside in liquid droplets nucleated at the centrosome. (A) Representative images of CRISPR-integrated tdmRuby3-CK1 $\alpha$ , tdmRuby3-GSK3 $\beta$ , and Axin1-tdmRuby3 cells. (Insets) Close-up views of singular perinuclear puncta. (Scale bar, 10  $\mu$ m.) (B) Representative cells bearing the indicated DC component fixed and stained for endogenous  $\gamma$ -tubulin. (Scale bar, 10  $\mu$ m.) (C) Representative timelapse images from live cells bearing dox- and cumate-inducible Axin1 and APC cassettes under induction. Montages depict the same cell increasing its DC scaffold concentration through time. (Scale bar, 10  $\mu$ m.) (D) Representative cells bearing the indicated DC component fixed and stained for endogenous  $\gamma$ -tubulin. (Scale bar, 10  $\mu$ m.) (E) FRAP traces of mean puncta:cytoplasm fluorescence ratio for indicated DC components. Data are presented as mean  $\pm$  SEM normalized to extent of bleaching ( $n = 39, 20, 33, 17,$  and  $22$  for Axin1, APC, CK1 $\alpha$ , GSK3 $\beta$ , and  $\beta$ -cat, respectively). Individual FRAP traces were fit to the equation:  $f(t) = a(1 - e^{-bt})$  to obtain  $a$  and  $b$  parameters and half-max recovery time ( $\tau_{1/2}$ ). Mean  $\tau_{1/2}$  for each DC component is displayed on each plot.

### A Reactive Cahn–Hilliard Model Predicts Accelerated $\beta$ -Cat Processing upon Centrosomal Nucleation of DC Clients.

To understand the effect of centrosomal nucleation of DC components on  $\beta$ -cat processing, we simulated the processive phosphorylation of  $\beta$ -cat by DC kinases, using a reactive, multicomponent,

Cahn–Hilliard system (34, 35). We represented the function of DC scaffolds implicitly through the interaction parameters between kinases and  $\beta$ -cat (Fig. 3 A and B and SI Appendix, Fig. S3 A–D). Indeed, synthetic DC scaffolds with these simple attributes have been shown to rescue aberrant Wnt signaling (36).

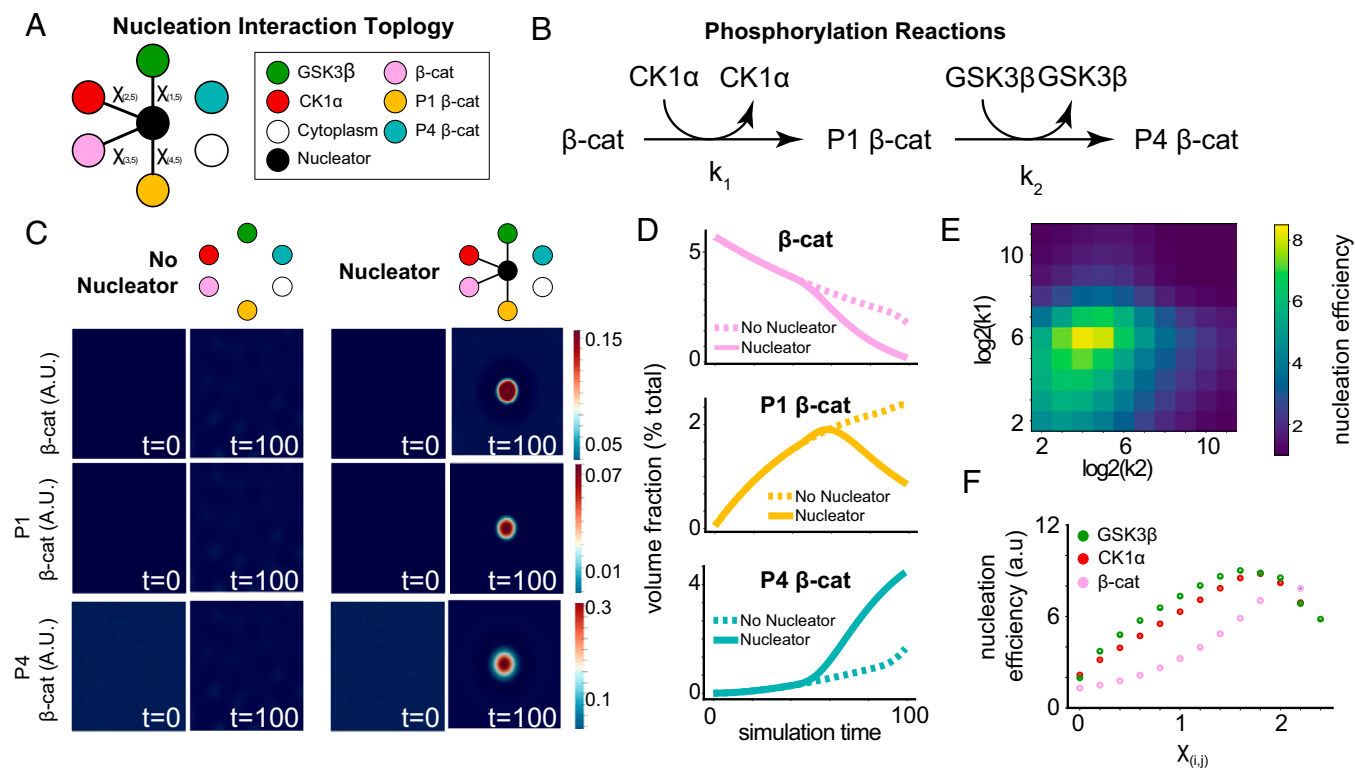


**Fig. 3.** In silico modeling of  $\beta$ -cat processing efficiency from a nucleated liquid droplet. (A) Nucleation interaction topology that describes the pairwise interactions between each component of the simulation. Connected components minimize free energy by mixing, and unconnected components either demix or remain in a noninteracting neutral state. (B) Schema describing the phosphorylation reactions and rates modeled in the simulation. (C) Simulation at steps 0 and 100 comparing a system with and without a centrosome. (D) Quantification of each form of  $\beta$ -cat with and without a centrosome. (E) Nucleation efficiency as a function of both rate parameters  $k_1$  and  $k_2$ . (F) Nucleation efficiency in simulations as a function of the interaction parameters between a single client and the cytoplasm.

To test the effects of nucleation on  $\beta$ -cat processing, we compared simulations in the presence and absence of a nucleation region (Fig. 3C). We found that, for systems that did not spontaneously phase separate, mimicking the endogenously expressed conditions observed above, DC components localized into a single droplet surrounding the nucleator but did not spontaneously demix in its absence (Movies S4 and S5). We found that the nucleated system processed  $\beta$ -cat and its intermediates more quickly (Fig. 3D) over a wide range of nucleator sizes (SI Appendix, Fig. S3E). See *Materials and Methods* for a detailed discussion of nucleation parameter scan results. Notably, the nucleated system accelerated  $\beta$ -cat processing, increasing pathway efficiency (SI Appendix, Fig. S3F). This efficiency gain was maintained over a large range of reaction rates (Fig. 3E and SI Appendix, Fig. S3G). As expected, in systems with high reaction rates, the effect of nucleated phase separation is no longer observed.

Given our findings that nucleation drives efficient processing of  $\beta$ -cat, we hypothesized that  $\chi$ , the interaction parameter that drives phase separation, is a control parameter for  $\beta$ -cat processing. To determine the relationship between DC function and the interaction strength parameter, we systematically decreased the  $\chi$  between DC clients and the cytoplasm. We found that reducing condensation on the nucleator, through altering  $\chi$ , decreased the speed and efficiency of  $\beta$ -cat processing (SI Appendix, Fig. S3H and I, Fig. 3F, and Movie S6). Together, these results demonstrate that nucleation of DC components has the potential to increase  $\beta$ -cat processing and that a tunable control parameter of this process is the free energy of mixing.

**Optogenetically Driven Enrichment of Centrosomal GSK3 $\beta$  Condensates Rescues Hyperactivated Wnt Signaling.** In silico analysis of the DC indicates that processing efficiency in the presence of a nucleator is dependent on client condensation. Imaging of GSK3 $\beta$  showed relatively weak enrichment in centrosomal puncta compared to CK1 $\alpha$ , suggesting that increasing nucleation of GSK3 $\beta$  would increase the degradation rate of  $\beta$ -cat in vivo. Changing concentration alters both propensity to undergo LLPS and reaction rate (37) and therefore cannot be used to test the effect of nucleation on reaction rate. Optogenetic photocrosslinking domains can independently control intracellular LLPS at fixed concentrations via light-induced changes in valency between monomers (38, 39). Thus, we reasoned that an optogenetic tool that drives changes in free energy could isolate the effect of nucleation from biological function.

To test whether photocrosslinking increases partitioning to a nucleator, we fused the photooligomerizer Cryptochrome-2 (Cry-2) and eGFP to human GSK3 $\beta$  (“Opto-GSK3” hereafter) and stably transduced it into 293Ts (Fig. 4A). Upon light stimulation, Opto-GSK3 increased its centrosomal enrichment, doubling the mean centrosome:cytoplasm fluorescence ratio within 10 s of activation (Fig. 4B and C and Movie S7). Notably, activation of Opto-GSK3 strictly resulted in the formation of one or two perinuclear puncta and did not form extracentrosomal condensates, contrasting with results from studies using Cry2 alone (17). Thus, we found that illumination of Opto-GSK induced condensate formation only at the centrosome.

To determine whether increased centrosomal condensation of GSK3 $\beta$  controlled Wnt signal transmission, we activated Opto-GSK3 in cell lines with three distinct methods for increasing the cellular concentration of  $\beta$ -cat: ligand-induced, kinase inhibition, and dox-induced gene up-regulation. We found that Opto-GSK activation abolished both Wnt-3a-induced  $\beta$ -cat accumulation and transcriptional activation as measured by TOPFlash fluorescence

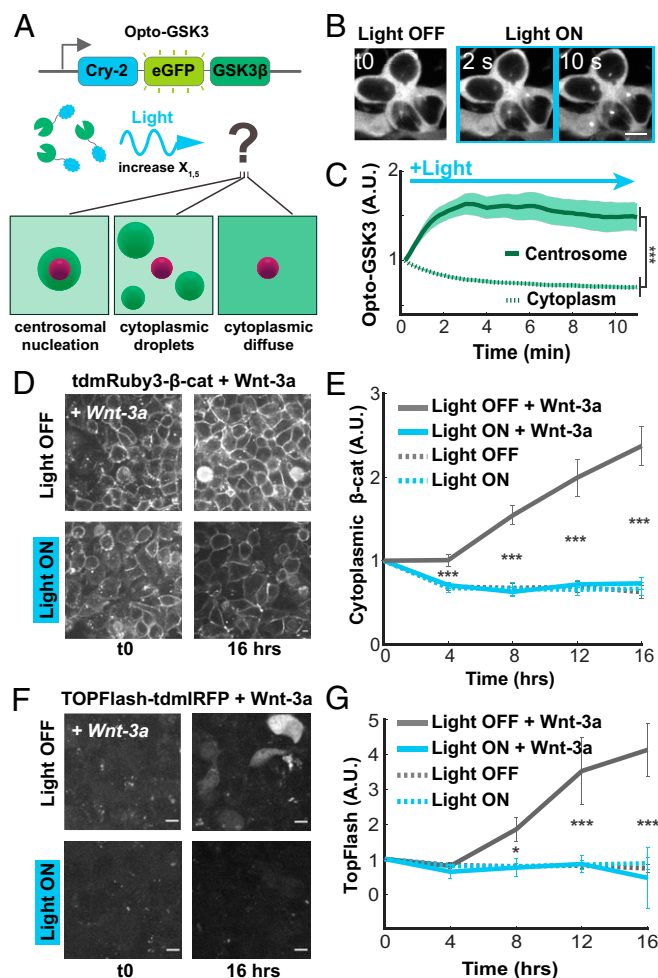


**Fig. 4.** Optogenetic clustering of GSK3 $\beta$  increases centrosomal droplet partitioning and suppresses Wnt pathway activation. (A) Schematic of Opto-GSK3 and possible spatial outcomes of blue light stimulation. (B) Representative images of cells bearing Opto-GSK3 responding to blue light stimulation. Montage depicts the same cells throughout the activation time course. (Scale bar, 10  $\mu$ m.) (C) Quantification of cells in B. Mean fluorescence fold change from t0 for each compartment  $\pm$  SEM ( $n = 20$  cells). (D) Representative images of cells bearing Opto-GSK3 + tdmRuby3- $\beta$ -cat following treatment with Wnt-3a. (Scale bar, 10  $\mu$ m.) (E) Quantification of cells in D. Mean fluorescence fold change from t0  $\pm$  SEM is shown ( $n = 20$  cells per condition). (F) Representative images of cells bearing Opto-GSK3 + TOPFlash-IRFP following treatment with Wnt-3a. (Scale bar, 10  $\mu$ m.) (G) Quantification of F. Mean fluorescence fold change from t0  $\pm$  SEM is shown ( $n = 24$  cells per condition).

(Fig. 4D and E). Control experiments comparing cells in light vs. dark confirmed that this was not due to light alone (SI Appendix, Fig. S4A and B). We observed a similar effect when analyzing total  $\beta$ -cat by Western blotting and immunofluorescence staining (SI Appendix, Fig. S4C–E). Given the modest accumulation of  $\beta$ -cat in response to Wnt-3a in 293Ts, we tested to see whether Opto-GSK3 clustering was sufficient to blunt  $\beta$ -cat accumulation induced by either CHIR or a Dox-inducible  $\beta$ -cat overexpression construct. Indeed, activation of Opto-GSK3 also inhibited both methods for driving  $\beta$ -cat accumulation in a light-dependent manner (SI Appendix, Fig. S4F–J). These results demonstrate that increasing DC client nucleation at the centrosome dictates Wnt signal transmission across a wide range of activation regimes.

**Centrosomal Enrichment of GSK3 $\beta$  Prevents Wnt Pathway Activation-Induced Differentiation of Embryonic Stem Cells.** Changes in  $\beta$ -cat concentration differentiate a variety of stem cell populations, including human embryonic stem cells (hESCs) (38, 40). Having determined that increased centrosomal nucleation

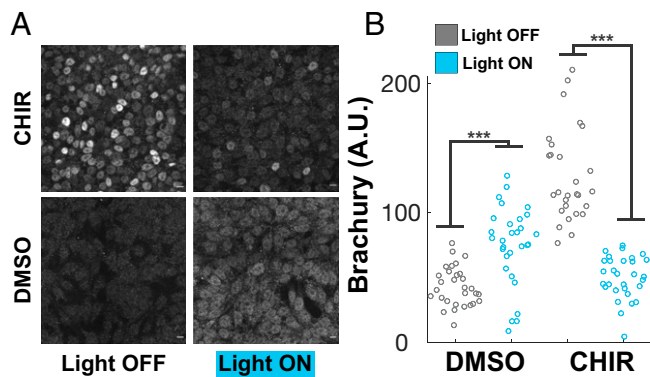


**Fig. 5.** Optogenetic clustering of GSK3 $\beta$  suppresses Wnt pathway-mediated differentiation of embryonic stem cells. (A) Representative images of H9 embryonic stem cells bearing Opto-GSK3 following 24 h in described conditions, fixed and stained for endogenous Brachyury. (B) Quantification of experiment from A. Mean nuclear fluorescence for cells measured in each condition is presented.

of GSK3 $\beta$  is sufficient to reduce  $\beta$ -cat accumulation and Wnt-responsive gene transcription in 293T cells, we wondered whether it was also sufficient to prevent the downstream differentiation of hESCs. Both CHIR and Wnt-3a induce hESC differentiation into mesoderm (41). To test whether centrosomal nucleation prevents differentiation, we expressed Opto-GSK3 in H9 hESCs and treated them with CHIR or dimethyl sulfoxide (DMSO) control in the presence or absence of activating blue light. Following stimulation, cells were fixed and stained for Brachyury (BRA) to assay for differentiation. In the dark, hESCs receiving CHIR responded robustly, displaying bright nuclear BRA compared to DMSO controls (Fig. 5 A). However, when stimulated with blue light, CHIR-treated cells showed significantly reduced levels of BRA staining compared to the dark controls, indicating that nucleation of GSK3 $\beta$  countered CHIR-induced differentiation into mesoderm (Fig. 5 A). Interestingly, we observed that BRA levels in DMSO and light condition were slightly, but significantly, higher than when in the dark, suggesting that overrepression of the Wnt pathway by Opto-GSK3 activation weakly promotes differentiation in hESCs as well (Fig. 5 B).

## Discussion

Building on recent discoveries suggesting that LLPS plays a role in DC structure, we sought to understand how the biophysics of DC proteins regulate DC function in live cells. Through a combination of superresolution microscopy, *in silico* modeling, and optogenetic methods to isolate and probe the phase diagram, we discovered that the mesoscale structure of the DC is a liquid condensate nucleated by the centrosome. The complementarity of these methods allowed us to identify a function for nucleation: acceleration of the catalytic action of DC proteins, thereby promoting efficient processing of  $\beta$ -cat.

The presence of many cytoplasmic Axin1 and APC droplets in mildly overexpressed cellular conditions (9) has been cited in support of the idea that DC scaffolds spontaneously phase separate at endogenous concentrations. Yet, because of the sensitivity of LLPS to concentration, we sought to examine the biophysics of DC components at endogenous concentrations. We found that, at low or endogenous levels, all DC components form dynamic assemblies with preferred localization to the centrosome. These results suggest that centrosomal nucleation lowers the concentration threshold for DC condensation.

Our results support a “molecular crucible” model of  $\beta$ -cat degradation, in which multivalent DC scaffolds concentrate DC clients

in nucleated droplets to increase  $\beta$ -cat phosphorylation rate. Assembly line models for  $\beta$ -cat degradation have been proposed (15, 42), and Axin1 polymerization has been observed to be ordered *in vitro* (28). Yet, others have shown that DC condensates display hallmarks of disorder, such as surface tension minimization, rapid fission/fusion (43), and responsiveness to concentration and interaction strength (9). Our results demonstrate that increased multivalency due to optogenetic photoclustering accelerates  $\beta$ -cat degradation, suggesting that DC function is responsive to disordered partitioning of DC clients into condensates.

We found that centrosomal DCs cease to concentrate  $\beta$ -cat under Wnt ON and GSK3 $\beta$  chemical inhibition, but the mechanism for this change remains unclear. Multiple DC components that bind  $\beta$ -cat—including Axin1, GSK3 $\beta$ , and CK1 $\alpha$ —are also binding partners of the Frizzled-LRP6 signalosome (44, 45), a known inhibitor of GSK3 $\beta$ 's phosphorylation of  $\beta$ -cat. Wnt-activated signalosomes may therefore compete with  $\beta$ -cat and/or GSK3 $\beta$  for DC proteins necessary for phosphorylation and degradation, resulting in the accumulation of nascent  $\beta$ -cat in the cytoplasm. For example, GSK3 $\beta$  phosphorylation is known to regulate APC's R2/B motif, which is critical for APC/Axin interaction and  $\beta$ -cat degradation (15). Alternatively, Dvl was recently found to regulate Wnt pathway activation via its affinity for Axin1's DIX domain (13), potentially “invading” and destabilizing Axin–Axin multimerization; such invasion of the DC could dilute Axin1 and its associated clients in the DC, reducing the phosphorylation rate of  $\beta$ -cat.

Our results raise an important question that may lead to the discovery of unknown potentiators of Wnt signal transduction: What is/are the nucleator(s) coupling the DC to the centrosome? Axin1 is known to associate with  $\gamma$ -tubulin (31) and is a substrate of PLK1, a kinase involved in centrosome duplication during cell cycle progression (23), suggesting that it is redundantly associated with the centrosome. APC is a regulator of microtubule stability and growth (24, 46), and its armadillo repeat region is sufficient to induce centrosomal localization (24). Multiple binding sites for DC scaffolds could localize the DC to the centrosome, increasing the robustness of droplet nucleation and enriching local client concentration. Notably, elimination of centrioles in developing mice and *Drosophila* embryos leads to only minor tissue-level defects in canonical Wnt signaling and overall morphology (47, 48), indicating that centrosomes are not essential for Wnt-mediated embryogenesis. We show that Axin is critically poised at the phase boundary, so it is possible that DC condensation is restored via simple up-regulation of this scaffold or the presentation of another nucleator through feedback mechanisms. Alternatively, another undiscovered DC nucleator that normally localizes to the centrosome may be sufficient to drive DC condensation when the centrosome is absent.

Finally, centrosomal nucleation of the DC suggests a potential function in coordinating cell cycle progression with Wnt signaling. We found two DC droplets in cells with duplicated centrosomes, suggesting that the DC is split along with centrosomes during mitosis. Nonnucleated droplets would be randomly partitioned into daughter cells, leading to potentially detrimental asymmetry in Wnt signaling capacity of the growing tissue. Cell cycle synchronization could be a method of reducing heterogeneity in Wnt-induced stem cell differentiations.

Overall, our studies suggest an integral role for LLPS nucleation in regulating the activity of membraneless organelles *in vivo*. The power of observing proteins in their endogenous contexts, coupled with the ability to precisely tune interaction strength without altering protein function or concentration, enables the functional dissection of membraneless organelles.

## Materials and Methods

**Cell Lines.** Human 293T cells were cultured at 37 °C and 5% CO<sub>2</sub> Dulbecco's Modified Eagle Medium, high glucose GlutaMAX (Thermo Fisher Scientific, 10566016) medium supplemented with 10% fetal bovine serum (Atlas Biologicals, F-0500-D), and 1% penicillin-streptomycin. The hiPSC WTC was gifted by the B.P. laboratory (purchased from Coriell). The hiPSCs were propagated on Matrigel-coated tissue culture plates using serum-free essential 8 (Gibco) culture conditions in standard environments consisting of 5% carbon dioxide at 37 °C. Experiments in hESC lines were performed using the H9 hESC cell line purchased from the William K. Bowes Center for Stem Cell Biology and Engineering at University of California, Santa Barbara (UCSB). Cells were grown in mTeSR Plus medium (Stem Cell Technologies) on Matrigel (Corning)-coated tissue culture dishes and tested for mycoplasma in 2-mo intervals.

**Cloning of PiggyBac Transposase and Lentiviral Overexpression Constructs.** The pPig\_H2B-mTagBFP2::t2A::Cas9-Avidin was constructed via subcloning human H2B, mTagBFP2, and Cas9-Avidin provided by M.Z.W. into an expression vector bearing a cytomegalovirus CMV promoter and flanking PiggyBac transposase-compatible inverted terminal repeats using Gibson Assembly (New England Biolabs Inc., E2611L) according to supplier instructions. Each of the PCR fragments used was amplified using the following primers:

PiggyBac (CMV) Backbone fwd: tgaccgcccccac rev: ggtaagctttttgcaaaagcc taggcc. H2B + 18AA linker fwd: cctaggtctttgcaaaagcttaccatgcccagagccagcgaagtc rev: GCATATTTCTGTAGGATTCACATCacCagTatGtcCgcCggAg. mTagBFP2 fwd: ATGAGTGAACATCATCAAGGAAATATGCACATG rev: CGTCCCGCAGGTCAACAACTTCCGGACCTTCTCCGCTCCACTTATGAGCTTATGGCCGAGTTTGTCTG. 3'X-Flag-NLS-Cas9-HA-Avidin fwd: GGAAGTTGTGACCTGCGGGGACGTGGAAGAAAACCCGGTCCAgactataa ggaccacgacggagactac rev: gctgcgggtgctggggcggcgtcagcagccagcgcag

XLone-Axin-tdmRuby3 was constructed via PCR and Gibson Assembly, subcloning from the following constructs: Flag-Axin1 purchased from Addgene (#109370), tdmRuby3 from M.Z.W. into XLone-GFP purchased from Addgene (#96930) containing-3'<sup>UTR</sup> gen tet ON-responsive promoter, and EF1 $\alpha$ -driven Blasticidin selection cassette. The following primers were used: XLone Backbone fwd: taactagtagaccacctccccctg, rev: ggtacctttacgagggtaggaagtgg, human Axin1 fwd: cacttctacctctgaaaggtaccatgaatccaagagcaggggtttccc, rev: CCATgctCCgCgCCTACTACGcCgtccaccttccctttgctgagtc, 7AA link- tdmRuby3 fwd: GgCgGTAGTGcGcGcGgAagcATGGTTAGCAAAGGGGAGGAGC, rev: gcaggggaggtggtactagttactCTGTACAGCTGCTCCATGCC

XLone-bCat-tdmRuby3 was constructed via PCR and Gibson Assembly, subcloning from the following constructs: XLone-Axin-tdmRuby3 (above) and Human Beta-catenin GFP purchased from Addgene (#71367). The following primers were used: XLone Backbone fwd: GgCgGTAGTGcGcGcGgAagcATGGTTAGCAAAGGGGAG GAGC, rev: ggtacctttacgagggtaggaagtgg, human bcat fwd: cacttctacctctgaaaggtaccatgactcaagctgtaggagttg, rev: CCATgctCCgCCgCCTACTACgCCcagctcagtt caaacaggccagc

The pPig\_CuO-APC-tdmIRFP670::CymR was constructed via PCR and Gibson Assembly from the following constructs: pCuo CA Rac1 CMV + cumate operon purchased from Addgene (#84643), human APC open reading frame (ORF) purchased from Addgene (#16507), tdmirfp670nano from M.Z.W., and human ubiquitin C-driven CymR Cuo repressor purchased from Addgene (#119907) into pPig-Hygro transposase backbone from M.Z.W. PCR fragments were amplified using the following primers:

pPig-Hygro Backbone fwd: GGACGTGGAAGAAAACCCGGTCCAatgggtaaaaagcctg aactaccgc, rev: cattcacagggctcagactagaagc, Cuo + CMV fwd: ctgtactgtcagcctgtggaatgcttataactacgtaaatgccccg, rev: actgatcatatgaagctgcagcagcattcgtacagcagcagctgactag, APC fwd: atgctgagcctcatatgatcagttgtaaaagcaag, rev: CCATgctCCgCCgCCTACTACgCCaacagatgtcacaagtaagaccagaag, 7AAlinker-tdmirfp670nano fwd: GgCgGTAGTGcGcGc, rev: ggcgcaaaacccggcgagggccttGGACTGCTGATTGCAATGCCAACTAC, UbC-CymR-V5-T2A fwd: ggcctccgcccggg, rev: TGGACCCGGGTTTTCTCCAGTCCCCGAGTCAACAACTCCCGACCTTCTCCG CTCCCgtagaatcagaccagggagag

The pLV\_Cry2-tdeGFP-GSK3b was obtained via synthesis and cloning services provided by Vector Builder Inc. Full details are available upon request, but, briefly: primary plasmids containing *Arabidopsis thaliana*, tdmIRFP from M.Z.W.

and human GSK3 $\beta$  purchased from Addgene (#16260) ORFs were supplied to VectorBuilder for cloning and EF1 $\alpha$ -driven expression into third-generation lentiviral backbone. Vectorbuilder provided the desired final, sequenced plasmid.

The pPig\_8XTOP\_tdmIRFP\_Puro was constructed via PCR and Gibson Assembly from the following constructs: pPig\_H2B-mTagBFP2::t2A::Cas9-Avidin (above), M50 Super 8x TOPFlash purchased from Addgene (#12456), and codon-optimized tandem (td) IRFP ordered from Twist Biosciences as overlapping gene fragments with the sequences:

ATGGCTGAAGGCAGCGTGGCCGACAGCCAGACCTTTGACTTGTGACGATGAACCAATC  
CACATACCGGGGCAATACAACCTCATGGTCTCTCTGCGCTGTGCGGACATGACTA  
TAGTGGCCGGCTCTGACAACCTGCGGAATTGACCGGACTGTACTATGGGGCGTTGATTG  
GGCGCTCTCCGCTGATGATTGATTCCGAGACACATAAGGCTTACTATAGCCCTCG  
CCGAACCAAGGGGCTCCGCTCGGCTCTATAAACAGTTGGTTACGATGCGAAAG  
ATGCTGGGTTTATTGATGCTGATCGCCACGATCACTTATCTTCTTGAAGGACCAATT  
CCCCTCAACGGGACGTTGCGGAACCCCAAGCTTCTTTAGAAGGACCAATTGACCCAT  
AAGGCGCTTCAGGCCGAGACATTGGAGTCCGCGTGTGCGGACGAGCGCAG  
GAAGTACGAAAGATCACGGGATTTGACCGGTTATGATTACAGATTGCTGATGATT  
CTCCGGGGAAGTCTCGCGGAGGATCGGTGTGCGAAGTGGAAAGCAAGCTTGGTT  
TGATTACCCCGCATCTACGGTCCGCGCAAGCGAGGAGACTGTATACGATAAACC  
CAGTGAGGATCATACTGACATAAATTATAGACCGTTCCCGTTACGCCAGCCTGAA  
CCCCGTACAGGCAGGCAATAGACTGTCTTTGCAATCTCGGTCAGTCTCACCTG  
TTACCTCGAGTTTATGAGGAACATAGGGATGATGGACGATGACATCTCAATCTG  
AGAGGTGAACGCTCTGCGGACTTATTGTTGTATCATCGCACACCGTATTACGTTGACC  
TTGATGTCGCGCAGGCTCGCAACTCGTAGCTCAAGTATTGGCTGCGAGATCGGTTAT  
GGAGGAAAGCGGTATGGGACTGGGAGTACAGGTAGCGGACGCTTATGTTGCCACTCC  
and

TAGCGGACGCTTACTGTTGACCTCCATGGCAGAAGGGTCCGTAGCAAGGCAACCTGACT  
TGTTGACTGTGATGATGAACCGATTACATCTCTGGAGCAATCAACCGCATGGGCTGCT  
CCTGCTTTGGCAGCGGACATGACGCTGCTCGGGCTCCGATAAATCCCGAGTTGA  
CGGCTTTGGCGATAGGAGCCCTGATAGCCGCTCAGCCGCTGACGTTATCGATAGCG  
AAACGCATAACCGGCTTACAATCGCTTGGCTGAACCGGGCGCGGCGTGGAGCA  
CCGATTACTGTAGGCTTACAATGAGAAAGACCGGCTTATCGGTCATGGCACC  
GACATGACCGCTGATTTCTGGAATTGGAGCCCCGACGCGGATGAGCCGAACCA  
CAGGCTTCTCCGCGCACTAATCCGCAATTAGGAGACTGACGGCAGCTGAGACTTT  
GGAATCAGCATGCGCGGAGCTGCACAAGAAGTCCGAAAATACCGGTTTGGACCGA  
GTCATGATCTATAGATTCGCGAGCGATTTCTCAGGAGAAGTTATGGGAAGACCGATG  
CGCGGAGGTAGAATCTAAGCTTGGGTTGCACTACCCGCTCCACCGTCCGCGCA  
CCGACGCGCTCTATACCTAATCCGTTGCGGATCAITCAGATATAAATACCGGCC  
TGACTCTGTGACACCGGATTTGAACTCTGTGCGGCGCCAGCATAGACTCAGCTTCC  
GCTATATTGCGATCTGTGTCACCGGCTCCACTCGAGTTTATGAGGAATATAGGCATGAT  
GGTACAATGTCCATTTCTTCCGGGTTGAACGCTTTGGGCTCATGTTTGTCCACC  
ATCGAACCCGATTATCTGATCTGACGCGCAGACAGGCATGTGAGTTGTGCTCAG  
GTACTCGTTGCGAGATAGGGTAATGAGGAG

PCR fragments were amplified using the following primers:

PiggyBacPuro backbone fwd: ACCTGCGGGGACGTGGAAGAAAACCCGGTCCAat  
gaccagtagcaagccagcgtg,  
rev: cattcacagggctcagactagaagcaaaag.  
8x TOPFlash fwd: ctgtactgtcagcctgtggaatgagtgagcaggtccagaacattctc,  
rev: GTCGGGCCAGCTGCTTCCAGCCTAGTggtgctttaccaagcagcagc.  
tdIRFP1 fwd: ATGGCTGAAGGCAGCTGGC,  
rev: GGAGGTGCCACTAGAGCTGC. tdmIRFP2  
fwd: TAGCGGACGCTTACTGTTGAC,  
rev: GGTITTTCTCCAGTCCCCGAGGTCAACAACTCCGCGACCTTCTCCGCTCCCTCT  
CCATACCCCTATCTGCCAAGCG

All above constructs were transformed into Top10 competent cells prepared using Mix & Go *E. coli* Transformation Kit and Buffer Set (Zymo Research #T3002), cultured on lysogeny broth agar plates to select for antibiotic resistance using standard workflows for molecular cloning and DNA production (49). Plasmid DNA was purified using the Zippy Plasmid Miniprep kit (Zymo Research #D0436). In addition to antibiotic selection, constructs were verified via Sanger sequencing using primers targeting fusion junctions of relevant construct domains.

**Lentiviral Production and Transduction.** Production of lentivirus carrying opto-GSK3 was accomplished using a cotransfection of pLV\_Cry2-tdeGFP-GSK3b,



pCMV dR8.91 (obtained from Jared Toettcher's Lab at Princeton University, Princeton, NJ) and pMD 2.G at a 1:0.88:0.11 mass ratio using standard PEI-based transfection procedures (50). Cells were incubated for 24 h before replacing with fresh media and allowing for lentiviral production for an additional 48 h. Supernatant was harvested, filtered through a 0.22- $\mu$ m filter and added to plated cells for transduction. Note that all steps for lentiviral production, transduction, and subsequent maintenance of cell lines were carried out in the presence of far-red light or the complete absence of light in an attempt to eliminate the possibility of Cry-2 opto-GSK3 clustering interference with cell growth or virus production.

**Construction of CRISPR gRNA Constructs and Homology-Directed Repair Templates.** Genomic edits in 293Ts were carried out in cells constitutively expressing Cas9 to maximize editing efficiency.

**pCAB\_minimal guide RNA backbone.** A vector expressing guide RNA (gRNA) and Cas9 obtained from M.Z.W. was subcloned to remove the unnecessary Cas9 ORF via PCR using the following primers:

fwd: acgcgacctgtagc

rev: ctaatgcccgtacagggcgctgtgtacctctagaccattgtctgc,

assembled, cloned, purified, and verified as described in the previous section. The baseline pCAB\_minimal construct was then subsequently used for production of gRNAs targeting exon1 of the human genomic loci of CTNNB1, CSNK1a1, and GSK3B. Primers creating one to three (depending on protospacer adjacent motif site availability/predicted on/off-target editing scores) unique protospacers targeting the 50-bp window surrounding the first codon of each gene were annealed and cloned into the pCAB\_minimal via BbsI digestion and ligation (New England Biolabs #R3539S, Takara #6023) using standard protocols (51). The following primers were used for sticky-end ligation of protospacers:

CTNNB1\_1 fwd: caccGTGAGTAGCCATTGTCACGC rev: aaacGCGTGGACAATGGCTACTCA

CTNNB1\_2 fwd: caccGTGAAAATCCAGCGTGGACAA rev: aaacTTGTCCACGCTGGATTTCac

CTNNB1\_3 fwd: caccGCGTGGACAATGGCTACTCA rev: aaacTGAGTAGCCATTGTCACGC

CSNK1a1\_1 fwd: caccGGCCAAGCCCCGACACCTCT rev: aaacAGAGGTGTCCGGGCTTGCC

CSNK1a1\_2 fwd: caccAGGCTGAATTCATTGTCCGA rev: aaacTCCGACAATGAATTCAGCCT

GSK3B fwd: caccCGAAGAGAGTGATCATGTCA rev: aaacTGACATGATCACTCTCTCC

AXIN1 gRNAs were ordered complete from IDT. Four different protospacer sequences were used (in separate reactions) with the same homology-directed repair (HDR) template to maximize chance of target locus cutting. Cells from each reaction were then pooled 7 d after transfection and subsequently enriched together.

Protospacer sequences:

AXIN1\_1: GGCCGCTCTGCCGCTCTTG

AXIN1\_2: GTCTTTGAGGAGAAGATCAT

AXIN1\_3: gTCTTTGAGGAGAAGATCATC

AXIN1\_4: GGAGAAGATCATCGGCAAG.

**HDR templates.** Blunt-end PCR products were used in conjunction with gRNAs to template genomic edits containing desired knock-ins. Blunt-end, double-stranded HDR templates were created from templates obtained via DNeasy Blood and Tissue genomic prep (Qiagen, 69504) of the 293T cell line to be edited (see next section). PCR was conducted using primers targeting amplicons of a 500- to 1,000-bp window centered on the intended cut site. The following primers were used to amplify genomic loci homology regions:

tdmRuby3: GgCGGTAGTGgCGGGAagcATGGTTAGCAAAGGGGAGGAGCTTATAA  
GGAAAATATGAGAATGAAAGTTGTCATGGAAGGTTCAAGTGGCCATCAGTTAAATG  
TACAGGTGAAGGCGAGGGACGCCCTATGAAGGAGTCCAAATATGAGGATCAAAGTC  
ATAGAGGGAGGTCCTCTCCCTTCGCTCGATATCTCGCCACCTTTTCATGTATGGTT  
CAAGAACATTATCAAGTATCCTGCCGATATACAGACTCTTTAAGCAGTCATTCCAGAA  
GGTTCACTTGGGAACGAGTCACTAGGTATGAGGACGCGGGGTTGTACAGTAACAA  
GACACCTCTTGAAGATGGTGAAGTGGTCTACAACGTGAAGGTACCGGGGTTAATTC  
CCTCTAACGGCCCTGTATGCAAAGAAGACAAAGGTTGGAGGCAAAATACCGAGAT  
GATGTATCCTGCAGATGGTGGCTCGGGCTATACCGACATCGCTCTGAAGGTAGACG  
GCGGGGCCACCTCCATTGTAATTTGTAACCACTTACAGGTCTAAGAAGACCGTGGGTA  
ACATTAAGATGCCAGGGTTCATGCTGTCACCATAGATTGGAGCGATAGAAGAAAGC  
GACAACGAGACCTACGTCGTCAACGCGAAGTCCGAGTACCAAGTATCCAATCTCGG  
GGGAGGTATGGATGAACCTATAAAGGCGGATCCGGTGGTGTGTCGAAGGAGAAGAA  
CTGATCAAAGAGAATGAGGATGAAGGTGTGATGGAGGGCAGCGTCAACGGACAC  
CAATCAAGTGCACCGGAGAGGAGAAGGCAGACCATACGAGGGCGTGCAGACAAT  
GAGAATTAAGGTATCGAAGGGGACCACTGCCCTTTGCTTTCGACATCTGGCTACAA

GCTTCATGTACGGCAGCAGACCTTCATTAATACCCCGCTGACATCCCTGATTTTTCAA  
ACAAAGCTTCCCTGAGGGCTTTACCTGGAGAGAGTGACAAGATACGAAAGCAGGAGG  
CGTCGCACCCGTACACAGGATAACAAGCCTGGAGGACGGAGAAGTGGTGATAACGT  
CAAAGTCAGAGGAGTGAACCTTCCAGCAATGGCCCCGTGATCGAGAAAAAGACCAA  
GGCTGGAACTAACACAGAAATGATGATACCAGCCGACGGAGGACTGAGAGGATACA  
CAGACATTGCCCTCAAAGTGGATGGAGGAGGACATCTGCACTGCAACTTCGTACAACC  
TACAGATCCAAGAAAAAGTGGAAATATCAAGATGCTGCGTGCACGCCGTGGATCA  
CAGGCTGAAAGGATTGAGGAGTCCGATAATGAACATATGTGTCCAGAGGGAGGTG  
GCCCTCGTAAATACAGCAACTGGGGCGGCGCATGGACGAGCTGTACAAGGGGGGA  
TCAGGAGGgGgctct

CTNNB1 fwd: ATAAAAAGACATTTTTGTAAGGAGGAGTTTTACTGAAGTTCAGCAGTGA  
TGAGGCTGTGGTGTGAGTGTCTGGAGGAGACCATGAGGTCTGCGTTTCA CTAACCTGGTA  
AAAGAGGATATGGGTTTTTTGTGGGTGTAATAGTGACATTTAACAGGTATCCAGTGACTT  
AGGAGTATTAATCAAGCTAAATTTAAATCCTAATGACTTTTGATTAACTTTTTAGGGTATT  
TGAAGTATACCATCAACTGTTTTGAAAATCCAGCGTGGACAGGcGGTAGTGcGcGcG  
GAagc

rev: TAGGGAACACCTAACAGTTACTCACTGAATCAGTGGAAAGTGGTACTGCATCCAG  
GCTCCAGAAGCAGTCCAGACTAGATTCTGCTGGTGGCTT GTTGTCTTTACCAAG  
CCATTAGGAGGAGTGCAGAAAAATGGAGCAAAAGGTAGCCTGACAAGTAAAGCAGGAG  
AGAGGAAAGCAGGGGATCTCAGCCAGACTGGCTAATGCAACGAAGCAGAGCCCCA  
ATTCACTAAGATTAATGACACAACCTTGTAGTACCATagagCCCTCTGATCCCCC

Note that CTNNB1 homology arms were synthesized (requiring no genomic amplification step) and provided as a generous gift from Integrated DNA Technologies.

CSNK1a1fwd: CCAGCCCGCAGCTC rev: CTGACCTTTTAGGGAGACAGCG

GSK3B fwd: GATTGCCCTCTCTTTCTCTCTCC rev: CCAAATAATATCATATATCTC  
AATCAAGGTAATGAGACCG

The above amplicons were then used in a second round of PCR to obtain separate upstream and downstream homology arms that flanked desired knock-ins, and overlap extension was used to construct the final desired amplicons bearing tdmRuby3 and 7AA GS linker. The following primers were used:

Generic tdmRuby3 insert fwd: GgCGGTAGTGgCGGGAagcATGGTTAGCAAAGGG  
GAGGAGC, rev: agagCtCCTCTGATCCCCCTGTACAGCTGTCCATGCC

CSNK1a1 upstream homology arm rev: gctTCCgCCgCCACTACCgCCCTGAG  
AGACGAAGATGGAGGC

CSNK1a1 downstream homology arm fwd: GGGGGATCAGGAGGaGgctctATGG  
CGAGTAGCAGCGC

GSK3B upstream homology arm rev: gctTCCgCCgCCACTACCgCCGATCACT  
CTCTCGGAATCACC

GSK3B downstream homology arm fwd: GGGGGATCAGGAGGaGgctctATGTA  
GGGCGGCC

AXIN1 upstream homology arm fwd: CTCACCCACATGTGGTCAITGCAC

AXIN1 upstream homology arm rev: CGCAAAGTGGAGAAGGTGGAGCGGcGG  
TAGTGgCGGGAagc

AXIN1 downstream homology arm fwd: GGGGGATCAGGAGGaGgctctTGATA  
GGCTGGTGGGCTGGCC

AXIN1 downstream homology arm rev: CACCTGAAGCTGGCAGCAGG

Note that original upstream fwd and downstream rev primers listed above for isolating genomic loci were reused in the present step and thus not repeated here.

**CRISPR-Cas9 Fluorescent Tagging.** Bare 293T cells were first cotransfected using polyethyleniminePEI (50) with the H2B-mTagBFP2 vector and Super Piggy-Bac Transposase-expressing vector (System Biosciences Inc. #PB210PA-1) via polyethylenimine (Sigma #408727-100ML) transfection reagent and standard workflows (50). Cells were allowed 72 h following transfection to reach steady-state expression of integrated construct and were enriched via two rounds of fluorescence-activated cell sorting (FACS, SH800S, Sony Biotechnology) for cells fluorescent in the 450-nm excitation (blue) channel: a bulk enrichment to obtain a largely "positive" population and a second to obtain clonal populations. A high-expressing clone was expanded and used as a "chassis" cell line for subsequent CRISPR editing.

CRISPR chassis cells were then cotransfected with one of the constructed gRNA plasmids and respective HDR templates at a 2:1 HDR template:gRNA plasmid molar ratio and allowed 72 h to reach steady-state expression. Similar to the

**Table 1. Statistical Parameters**

<i>P</i> value range	Symbol
0.01 < <i>P</i> < 0.05	*
0.001 < <i>P</i> < 0.01	**
<i>P</i> < 0.001	***

All statistical tests were carried out on final grouped data points presented in figures using independent samples *t* tests (Matlab function "ttest2") except for *SI Appendix, Fig. S4D* which was the result of one-way ANOVAs.

process described above, cells were subject to two rounds of FACS (561-nm excitation, red laser) to obtain a clonal population. Knock-in validation was accomplished via a combination of fluorescence microscopy, genomic PCR, and sequencing (using primers for initial amplification of loci and construction of HDR templates). In the case of all intended knock-ins, spatiotemporal fluorescence expression of cell populations was binary (either fluorescent or not) and uniform (no detected variation in brightness or localization between fluorescent clones), suggesting that selected clones were broadly representative of overall edited populations.

**Development of Inducible Axin1, APC, and  $\beta$ -Cat Cell Lines.** The 293Ts were cotransfected as described in the previous section with PiggyBac and compatible Xlone-Axin-tdmRuby3 and pPig\_CuO-APC-tdmIRFP670::CymR expression cassettes. Seventy-two hours after transfection, cells were selected in 1  $\mu$ M Blasticidin (Invivogen, #ant-bl-05) and 100  $\mu$ g/mL Hygromycin B Gold (Invivogen, #ant-hg-1). Blast+/Hygro+ cells were then clonally sorted via FACS as described in the previous section to obtain a uniform population for experiments. For iPSCs, Both Piggyback and Donor plasmids were chemically transfected when cells reached 30% confluency using Lipofectamine Stem Transfection Reagent (manufacturer's protocol). Following transfection, Blasticidin selection (1  $\mu$ M) was initiated 5 d later. At the end of Blasticidin selection, 12 clones were manually picked under a dissection microscope and continuously cultured in Blasticidin (1  $\mu$ M) for an additional week. Upon fluorescence signal confirming successful integration, Blasticidin (1  $\mu$ M) treatment ceased, and one clone was chosen for the remaining experiments.

**Small Molecules.** CHIR 99021 (STEMCELL Technologies #72052) was resuspended in DMSO according to supplied manufacturer recommendations and diluted to 5 $\times$  concentrated stocks in culture medium immediately prior to use on cells. In all cases, CHIR was used at 10  $\mu$ M. Doxycycline hyclate (Sigma Aldrich #D9891-1G) was resuspended in phosphate-buffered saline (PBS) and diluted to 5 $\times$  desired concentration in culture medium prior to use. Stock cumate solution (System Biosciences #QM100A-1) was diluted to 5 $\times$  in culture medium prior to use.

The "Low" dose of Dox referred to in Fig. 2 C and D in the context of Axin and APC induction was 20 ng/mL concentration in culture medium, "High" dose was 200 ng/mL. "Low" dose of Cumate was 100 ng/mL, and "High" was 1mg/mL. The dose of Dox used in  $\beta$ -cat induction in *SI Appendix, Fig. S4 I and J* was 100 ng/mL.

**Wnt-3a Treatments.** Recombinant Human Wnt-3a (R&D Systems 5036-WN-010) was resuspended in PBS containing 0.1% bovine serum albumin according to supplied manufacturer recommendations and diluted to 5 $\times$  concentration

in culture medium immediately prior to use. In all cases, Wnt-3a was used at a final concentration of 1  $\mu$ g/mL.

**Antibodies, Immunofluorescence, and Western Blot.** Primary antibodies used for immunofluorescent markers of the centrosome were  $\alpha$ -GM130 (BD 610822, 1:1,000 dilution [dil.]) and  $\alpha$ - $\gamma$ -tubulin (Sigma Aldrich T5326-25UL, 1:1,000). The secondary used for both stains was  $\alpha$ -Ms-Alexa-488 (Invitrogen A28175, 1:1,000). Tissue fixation and staining was carried out using standard protocols using cold methanol (52). Immunofluorescent samples were imaged using confocal microscopy (see below). Antibodies used for Western blotting and immunofluorescence were  $\alpha$ - $\beta$ -catenin (Cell Signaling, #2698S, 1:1,000) and  $\alpha$ - $\beta$ -actin (Sigma, A3853, 1:1,000). Secondary antibodies used were  $\alpha$ -Gt-680RD and  $\alpha$ -Ms-800CW (Licor 926-6807 and 926-32212, respectively, both 1:10,000 dil.). Standard immunoblot procedures were used (53).

**Imaging.** All live and fixed cell imaging experiments were carried out using a Nikon W2 SoRa spinning-disk confocal microscope equipped with incubation chamber maintaining cells at 37  $^{\circ}$ C and 5% CO<sub>2</sub>. Glass-bottom culture plates (Cellvis #P96-1.5H-N) were pretreated with bovine fibronectin (Sigma #F1141) in the case of 293Ts or Matrigel in the case of H9 and iPSCs, and cells were allowed to adhere to the plate before subsequent treatment or imaging. FRAP was performed via custom Nikon NIS Elements JOBS function and 488-nm FRAP laser (Nikon LUN-F laser unit, 100-mW power output from the APC fiber tip).

**Optogenetic Stimulation.** Spatial patterning of light during timelapse fluorescence imaging sessions was accomplished via purpose-built microscope-mounted LED-coupled digital micromirror devices (DMDs) triggered via Nikon NIS Elements software. Stimulation parameters (brightness levels, duration, and pulse frequency) were optimized to minimize phototoxicity while maintaining continuous activation of Cry-2. For DMD-based stimulation on the microscope, the final settings for "Light ON" were 25% LED power ( $\lambda = 455$  nm), 2-s duration pulses every 30 s. For experiments that did not require frequent confocal imaging, cells were stimulated via a benchtop LED array purpose built for light delivery to cells in standard tissue culture plates ("OptoPlate") adapted from previously established designs (54). The same light delivery parameters were used for OptoPlate-based stimulation as for microscope-mounted DMDs. Light was patterned to cover the entire surface of intended wells of plates used, rather than a single microscope imaging field.

**Image Analysis.** All quantification of raw microscopy images was carried out using the same general workflow: background subtraction > classification > measurement > normalization > statistical comparison. Subcellular segmentation of nuclear fluorescence was performed via custom Matlab scripts using H2B-mTagBFP2 brightness, size, and circularity to mask objects. When experimental conditions did not permit segmentation via H2B-mTagBFP2 nuclear fluorescence (such as with live-cell optogenetic stimulation), cells were selected at random using custom ImageJ macro that generates random regions of interest (ROIs) (available upon request). Unless otherwise noted, mean fluorescent intensity of ROIs were measured and subsequently processed. Raw measurements were compiled, processed, and plotted via custom Matlab scripts, available upon request.

**Statistical Analysis.** Statistical parameters are provided in Table 1.

**Simulation Methods.** We used the Python-based FEniCS computing environment (<https://fenicsproject.org/>) to solve the modified Cahn-Hilliard partial

**Table 2. Representations of interaction parameters between indicated model system components**

Component variable	Component name	CH equation
$\phi_1$	GSK3 $\beta$	$\frac{\partial \phi_1}{\partial t} = M_1 \nabla^2 \mu_1$
$\phi_2$	CK1 $\alpha$	$\frac{\partial \phi_2}{\partial t} = M_2 \nabla^2 \mu_2$
$\phi_3$	$\beta$ -cat	$\frac{\partial \phi_3}{\partial t} = M_3 \nabla^2 \mu_3 - (k_{2,3} \cdot \phi_2 \cdot \phi_3)$
$\phi_4$	Phospho-S45 $\beta$ -cat	$\frac{\partial \phi_4}{\partial t} = M_4 \nabla^2 \mu_4 + (k_{2,3} \cdot \phi_2 \cdot \phi_3) - (k_{1,4} \cdot \phi_1 \cdot \phi_4)$
$\phi_5$	Phospho-S33/S37/S45/T41 $\beta$ -cat	$\frac{\partial \phi_5}{\partial t} = M_5 \nabla^2 \mu_5 + (k_{1,4} \cdot \phi_1 \cdot \phi_4)$
$\phi_6$	Cytoplasm	$\frac{\partial \phi_6}{\partial t} = M_6 \nabla^2 \mu_6$
$\phi_7$	Nucleator	$\frac{\partial \phi_7}{\partial t} = M_7 \nabla^2 \mu_7$

**Table 3. Binding actions of modeled DC components, provided with citations from which they were obtained**

Interaction	Behavior	Source
Scaffold to GSK3 $\beta$	Binding	Refs. 36 and 42
Scaffold to CK1 $\alpha$	Binding	Refs. 36 and 42
Scaffold to $\beta$ -cat	Binding	Ref. 42
Scaffold to P1 $\beta$ -cat	Binding	Ref. 11
Scaffold to P4 $\beta$ -cat	Neutral	Refs. 11 and 42
Scaffold to cytoplasm	Separating	This study
Scaffold to centrosome	Binding	This study and ref. 31

differential equations using the finite element method. In our simulation, we represent the volume fraction of each DC protein,  $\phi_i$ , as an incompressible volume such that  $\sum_{i=1}^N \phi_i = 1$  and approximate the reaction rates with spatially dependent analogs to well-mixed reactions using the simplified, non-state-dependent description of the second-order rate  $R_i = k_{ij}\phi_i\phi_j$ , with production and consumption denoted by the sign of  $k_{ij}$  (55, 56). The Cahn-Hilliard equation, in its general form, is a parabolic equation with first-order time derivatives, and second- and fourth-order spatial derivatives. To solve this equation using a standard Lagrange finite element basis, the equation is recast as two coupled second-order equations,

$$\frac{\partial \phi_i}{\partial t} = \nabla \cdot M(\nabla(\mu_i)) + R_i(k_{ij}, \phi_i, \phi_j)$$

$$\mu_i = \frac{\partial F}{\partial \phi_i} - \lambda \nabla^2 \phi_i,$$

where  $M_i$  is the mobility constant, with all DC components having the same diffusion rate,  $\lambda$  is the surface energy parameter that dictates the length of transition regions between domains, and  $F$  is the polynomial double-well description of the free energy,

$$F = \sum_{i=1}^{N-1} \sum_{j=2}^N \chi_{ij} \phi_i^2 \phi_j^2,$$

where  $\chi_{ij}$  describes interaction strength between DC proteins, the cytoplasm, and the centrosome. We modeled centrosomal nucleation as a region in the simulation with increased interaction strength as has been done previously to describe nucleation sites (57). To determine the size of this nucleation region, we measured the relative volume of centrosomally localized DC kinases and  $\beta$ -cat (SI Appendix, Fig. S3B), and  $R_i$  is the added reaction term such that

$$R_i(k_{ij}, \phi_i, \phi_j) = k_{ij}\phi_i\phi_j \text{ for the creation of } \phi_i$$

and

$$R_i(k_{ij}, \phi_i, \phi_j) = -k_{ij}\phi_i\phi_j \text{ for the consumption of } \phi_i.$$

The system is time discretized according to established methods (58). Assuming that the total free energy of the system decreases to a minimum with time, we use the built-in Newtonian solver in the FEniCS environment to approximate the forward evolution of the system in time. To represent the enzyme activities in the DC, we model only clients, with scaffolds existing implicitly as the interaction parameters between system components. Representations are given in Table 2.

**Interaction Parameter.** One of the key factors that tunes system behavior is the interaction parameter  $\chi$ . Assuming a system with constant temperature and pressure, the interaction parameter determines the free energy of the system.

1. A. Kusserow *et al.*, Unexpected complexity of the Wnt gene family in a sea anemone. *Nature* **433**, 156–160 (2005).
2. R. Nusse, H. Clevers, Wnt/ $\beta$ -catenin signaling, disease, and emerging therapeutic modalities. *Cell* **169**, 985–999 (2017).
3. H. Clevers, Wnt/ $\beta$ -catenin signaling in development and disease. *Cell* **127**, 469–480 (2006).
4. V. S. W. Li *et al.*, Wnt signaling through inhibition of  $\beta$ -catenin degradation in an intact Axin1 complex. *Cell* **149**, 1245–1256 (2012).
5. A. Cliffe, F. Hamada, M. Bienz, A role of Dishevelled in relocating Axin to the plasma membrane during wingless signaling. *Curr. Biol.* **13**, 960–966 (2003).
6. L. J. Bugaj, A. T. Choksi, C. K. Mesuda, R. S. Kane, D. V. Schaffer, Optogenetic protein clustering and signaling activation in mammalian cells. *Nat. Methods* **10**, 249–252 (2013).

When  $\chi$  is positive between two components, the system will tend to demix. If  $\chi$  is negative between two components, they will tend to mix. Lastly, if  $\chi$  is neutral, the two components are interactionless. For simplicity, we limited interactions to one of three types: binding ( $\chi \approx -0.1$ ), neutral ( $\chi \approx 0$ ), and separating ( $\chi \approx 2$ ). As noted above, we represent the binding action of DC scaffolds implicitly. Scaffold interactions are taken to be of similar strength and were obtained from literature values described in Table 3.

Given that the APC/Axin interacts with the DC proteins, the following interaction constants were selected for the system with implicit Axin. We set mixing = 2.0, neutral = 0.0, and demixing =  $-0.1$ .

**Simulation Flow.** First, all parameters are defined ( $\chi$ ,  $\lambda$ ,  $\partial t$ , and  $M$ ). We generate a grid mesh with closed boundary conditions to mimic the closed system within a cell. A layer is generated for each simulated component, and  $\pm 5\%$  noise of the initial value is added to induce inhomogeneities. The FEniCS package partial differential solver is called to generate the chemical potential with respect to each component. The final step is to define the output file path and then use the built-in Newton solver to generate the simulation. The simulations are then rendered using Paraview software. A detailed Python notebook of the simulations is available on <https://github.com/MZWLlab/Lach2022>.

**Nucleation Efficiency Parameter Scans.** We defined the nucleation efficiency of  $\beta$ -cat processing for a given simulation by comparing the ratio of the integrated P4- $\beta$ -cat to  $\beta$ -cat between identical simulations with and without a nucleator (SI Appendix, Fig. S3F). This allowed us to test the sensitivity of a single metric to alterations in our model's parameters. In Fig. 3E, we independently altered the simulated phosphorylation rates of CK1 and GSK3, K1 and K2, to examine how nucleation efficiency was changed. Our findings are intuitive, in that the faster K1 and K2 are, the less nucleation leads to an efficiency gain for the system. In Fig. 3F, we examined nucleation efficiency as a function of the free energy of binding between each of the individual DC clients and the cytoplasm, finding that, in general, increasing the free energy penalty of client-cytoplasm mixing drove greater accumulation of clients at the nucleator (Movie S6) and also increased the nucleation efficiency.

**Data, Materials, and Software Availability.** ImageJ macros for ROI generation and measurement are available upon request. Raw measurements were compiled, processed, and plotted via custom Matlab scripts, available upon request. Full details on creating pLV\_Cry2-tdeGFP-GSK3b are available upon request. A detailed Python notebook of the simulations is available on GitHub at <https://github.com/MZWLlab/Lach2022> (59). All data used to generate figures and graphs are provided in the present document or supplementary materials.

**ACKNOWLEDGMENTS.** We thank Ken Kosik and Denise Montell for guidance on the project direction; Cassidy Arnold and Erik Hopkins for technical support with maintenance, enrichment, and assaying clonal cell lines; and Imogen Rawlings-Green, Natalie Tjahjadi, and Mark Lu for support with data analysis. We thank the Eunice Kennedy Shriver National Institute of Child Health and Development for funding R.S.L. (Award 1F31HD106900-01A1), and Cancer Research Coordinating Committee (CRCC), 2021-22 Faculty Seed Grant (UCSB, C22CR4129) for funding the work.

Author affiliations: <sup>a</sup>Department of Molecular, Cellular, and Developmental Biology, University of California, Santa Barbara, CA 93106; <sup>b</sup>Neuroscience Research Institute, University of California, Santa Barbara, CA 93106; <sup>c</sup>Biomolecular Science and Engineering, University of California, Santa Barbara, CA 93106; <sup>d</sup>Department of Mechanical Engineering, University of California, Santa Barbara, CA 93106; and <sup>e</sup>Center for BioEngineering, University of California, Santa Barbara, CA 93106

7. J. Nong *et al.*, Phase separation of Axin organizes the  $\beta$ -catenin destruction complex. *J. Cell Biol.* **220**, e202012112 (2021).
8. D. M. Roberts *et al.*, Defining components of the  $\beta$ catenin destruction complex and exploring its regulation and mechanisms of action during development. *PLoS One* **7**, e31284 (2012).
9. K. N. Schaefer *et al.*, Supramolecular assembly of the beta-catenin destruction complex and the effect of Wnt signaling on its localization, molecular size, and activity in vivo. *PLoS Genet.* **14**, e1007339 (2018).
10. W. Kan *et al.*, Limited dishevelled/Axin oligomerization determines efficiency of Wnt/ $\beta$ -catenin signal transduction. *eLife* **9**, e55015 (2020).
11. K. N. Schaefer, M. Peifer, Wnt/ $\beta$ -catenin signaling regulation and a role for biomolecular condensates. *Dev. Cell* **48**, 429–444 (2019).

12. D. M. Roberts *et al.*, Deconstructing the  $\beta$ -catenin destruction complex: Mechanistic roles for the tumor suppressor APC in regulating Wnt signaling. *Mol. Biol. Cell* **22**, 1845–1863 (2011).
13. K. Yamanishi *et al.*, A direct heterotypic interaction between the DIX domains of Dishevelled and Axin mediates signaling to  $\beta$ -catenin. *Sci. Signal.* **12**, eaaw5505 (2019).
14. C. J. Bashor, N. C. Helman, S. Yan, W. A. Lim, Using engineered scaffold interactions to reshape MAP kinase pathway signaling dynamics. *Science* **319**, 1539–1543 (2008).
15. M. I. Pronobis, N. M. Rusan, M. Peifer, A novel GSK3-regulated APC:Axin interaction regulates Wnt signaling by driving a catalytic cycle of efficient  $\beta$ -catenin destruction. *eLife* **4**, e08022 (2015).
16. S. F. Shimobayashi, P. Ronceray, D. W. Sanders, M. P. Haataja, C. P. Brangwynne, Nucleation landscape of biomolecular condensates. *Nature* **599**, 503–506 (2021).
17. Y. Shin *et al.*, Spatiotemporal control of intracellular phase transitions using light-activated optodroplets. *Cell* **168**, 159–171.e14 (2017).
18. S. C. Weber, C. P. Brangwynne, Inverse size scaling of the nucleolus by a concentration-dependent phase transition. *Curr. Biol.* **25**, 641–646 (2015).
19. Y. Lin *et al.*, Narrow equilibrium window for complex coacervation of tau and RNA under cellular conditions. *eLife* **8**, e42571 (2019).
20. T. Mora, W. Bialek, Are biological systems poised at criticality? *J. Stat. Phys.* **144**, 268–302 (2011).
21. S. M. Vora, J. S. Fassler, B. T. Phillips, Centrosomes are required for proper  $\beta$ -catenin processing and Wnt response. *Mol. Biol. Cell* **31**, 1951–1961 (2020).
22. D. D. Kaplan, T. E. Meigs, P. Kelly, P. J. Casey, Identification of a role for beta-catenin in the establishment of a bipolar mitotic spindle. *J. Biol. Chem.* **279**, 10829–10832 (2004).
23. K. Ruan *et al.*, PLK1 interacts and phosphorylates Axin that is essential for proper centrosome formation. *PLoS One* **7**, e49184 (2012).
24. C. Lui, M. T. S. Mok, B. R. Henderson, Characterization of adenomatous polyposis coli protein dynamics and localization at the centrosome. *Cancers (Basel)* **8**, 47 (2016).
25. I. Cunha-Ferreira *et al.*, The SCF/Slimb ubiquitin ligase limits centrosome amplification through degradation of SAK/PLK4. *Curr. Biol.* **19**, 43–49 (2009).
26. S. Munemitsu *et al.*, The APC gene product associates with microtubules in vivo and promotes their assembly in vitro. *Cancer Res.* **54**, 3676–3681 (1994).
27. S. Alberti, A. Gladfelter, T. Mittag, Considerations and challenges in studying liquid-liquid phase separation and biomolecular condensates. *Cell* **176**, 419–434 (2019).
28. T. Schwarz-Romond, C. Metcalfe, M. Bienz, Dynamic recruitment of axin by Dishevelled protein assemblies. *J. Cell Sci.* **120**, 2402–2412 (2007).
29. Z. C. Elmore, R. X. Guillen, K. L. Gould, The kinase domain of CK1 enzymes contains the localization cue essential for compartmentalized signaling at the spindle pole. *Mol. Biol. Cell* **29**, 1664–1674 (2018).
30. B. C. Mbom, W. J. Nelson, A. Barth,  $\beta$ -catenin at the centrosome: Discrete pools of  $\beta$ -catenin communicate during mitosis and may co-ordinate centrosome functions and cell cycle progression. *BioEssays* **35**, 804–809 (2013).
31. K. Fumoto, M. Kadono, N. Izumi, A. Kikuchi, Axin localizes to the centrosome and is involved in microtubule nucleation. *EMBO Rep.* **10**, 606–613 (2009).
32. B. G. O'Flynn, T. Mittag, A new phase for enzyme kinetics. *Nat. Chem. Biol.* **17**, 628–630 (2021).
33. D. T. McSwiggen, M. Mir, X. Darzacq, R. Tjian, Evaluating phase separation in live cells: Diagnosis, caveats, and functional consequences. *Genes Dev.* **33**, 1619–1634 (2019).
34. C. Liu *et al.*, Control of beta-catenin phosphorylation/degradation by a dual-kinase mechanism. *Cell* **108**, 837–847 (2002).
35. C. J. Fiol, A. Wang, R. W. Roeske, P. J. Roach, Ordered multisite protein phosphorylation. Analysis of glycogen synthase kinase 3 action using model peptide substrates. *J. Biol. Chem.* **265**, 6061–6065 (1990).
36. M. I. Pronobis, N. Deutch, V. Posham, Y. Mimori-Kiyosue, M. Peifer, Reconstituting regulation of the canonical Wnt pathway by engineering a minimal  $\beta$ -catenin destruction machine. *Mol. Biol. Cell* **28**, 41–53 (2017).
37. A. A. M. André, E. Spruijt, Liquid-liquid phase separation in crowded environments. *Int. J. Mol. Sci.* **21**, 5908 (2020).
38. A. B. Rosenbloom *et al.*,  $\beta$ -Catenin signaling dynamics regulate cell fate in differentiating neural stem cells. *Proc. Natl. Acad. Sci. U.S.A.* **117**, 28828–28837 (2020).
39. D. Bracha *et al.*, Mapping local and global liquid phase behavior in living cells using photo-oligomerizable seeds. *Cell* **175**, 1467–1480.e13 (2018).
40. R. C. Lindsley, J. G. Gill, M. Kyba, T. L. Murphy, K. M. Murphy, Canonical Wnt signaling is required for development of embryonic stem cell-derived mesoderm. *Development* **133**, 3787–3796 (2006).
41. M. Thomson *et al.*, Pluripotency factors in embryonic stem cells regulate differentiation into germ layers. *Cell* **145**, 875–889 (2011).
42. E. Lee, A. Salic, R. Krüger, R. Heinrich, M. W. Kirschner, The roles of APC and axin derived from experimental and theoretical analysis of the Wnt pathway. *PLoS Biol.* **1**, e10 (2003).
43. T.-M. Li *et al.*, Multivalent tumor suppressor adenomatous polyposis coli promotes Axin biomolecular condensate formation and efficient  $\beta$ -catenin degradation. *Sci. Rep.* **10**, 17425 (2020).
44. X. Zeng *et al.*, Initiation of Wnt signaling: Control of Wnt coreceptor Lrp6 phosphorylation/activation via frizzled, dishevelled and axin functions. *Development* **135**, 367–375 (2008).
45. C. Niehrs, J. Shen, Regulation of Lrp6 phosphorylation. *Cell. Mol. Life Sci.* **67**, 2551–2562 (2010).
46. C. Lui, C. Ashton, M. Sharma, M. G. Brocardo, B. R. Henderson, APC functions at the centrosome to stimulate microtubule growth. *Int. J. Biochem. Cell Biol.* **70**, 39–47 (2016).
47. H. Bazzi, K. V. Anderson, Acentriolar mitosis activates a p53-dependent apoptosis pathway in the mouse embryo. *Proc. Natl. Acad. Sci. U.S.A.* **111**, E1491–E1500 (2014).
48. R. Basto *et al.*, Flies without centrioles. *Cell* **125**, 1375–1386 (2006).
49. B. Perbal, *A Practical Guide to Molecular Cloning* (John Wiley, New York, 1988).
50. Addgene: General transfection. <https://www.addgene.org/protocols/transfection>. Accessed 28 June 2021.
51. Addgene: Zhang lab CRISPR page. <https://www.addgene.org/crispr/zhang>. Accessed 28 June 2021.
52. Abcam: Immunocytochemistry and immunofluorescence protocol. <https://www.abcam.com/protocols/immunocytochemistry-immunofluorescence-protocol>. Accessed 29 June 2021.
53. Abcam: Western blot protocol. <https://www.abcam.com/protocols/general-western-blot-protocol>. Accessed 29 June 2021.
54. L. J. Bugaj, W. A. Lim, High-throughput multicolor optogenetics in microwell plates. *Nat. Protoc.* **14**, 2205–2228 (2019).
55. J. Berry, C. P. Brangwynne, M. Haataja, Physical principles of intracellular organization via active and passive phase transitions. *Rep. Prog. Phys.* **81**, 046601 (2018).
56. J. F. Lutsko, Mechanism for the stabilization of protein clusters above the solubility curve: The role of non-ideal chemical reactions. *arXiv [Preprint]* (2016). <https://doi.org/10.48550/arXiv.1601.08043>. Accessed 20 January 2022.
57. J. Berry, S. C. Weber, N. Vaidya, M. Haataja, C. P. Brangwynne, RNA transcription modulates phase transition-driven nuclear body assembly. *Proc. Natl. Acad. Sci. U.S.A.* **112**, E5237–E5245 (2015).
58. M. W. Scroggs, J. S. Dokken, C. N. Richardson, G. N. Wells, Construction of arbitrary order finite element degree-of-freedom maps on polygonal and polyhedral cell meshes, *ACM Transactions on Mathematical*. <https://dl.acm.org/doi/10.1145/3524456>. Accessed 20 January 2022.
59. JollyWanderer, Nucleation of the destruction complex on the centrosome accelerates degradation of  $\beta$ -catenin and regulates Wnt signal transmission (2022). GitHub. <https://github.com/MZWLab/Lach2022>. Deposited 17 August 2022.